




# Calibration of a multi-anvil high-pressure apparatus to simulate planetary interior conditions

J. S. Knibbe<sup>1\*</sup> , S. M. Luginbühl<sup>1</sup>, R. Stoevelaar<sup>1</sup>, W. van der Plas<sup>1</sup>, D. M. van Harlingen<sup>1</sup>, N. Rai<sup>2</sup>, E. S. Steenstra<sup>1</sup>, R. van de Geer<sup>1</sup> and W. van Westrenen<sup>1</sup>

\* Correspondence: [j.s.knibbe@vu.nl](mailto:j.s.knibbe@vu.nl)

<sup>1</sup>Faculty of Science, Vrije Universiteit Amsterdam, Amsterdam, the Netherlands

Full list of author information is available at the end of the article

## Abstract

This paper presents the setup and pressure calibration of an 800-ton multi-anvil apparatus installed at the Vrije Universiteit (Amsterdam, the Netherlands) to simulate pressure-temperature conditions in planetary interiors. This high-pressure device can expose cubic millimeter sized samples to near-hydrostatic pressures up to ~ 10 GPa and temperatures exceeding 2100 °C. The apparatus is part of the Distributed Planetary Simulation Facility (DPSF) of the EU Europlanet 2020 Research Infrastructure, and significantly extends the pressure-temperature range that is available through international access to this facility.

**Keywords:** High pressure, Multi-anvil, Experimental petrology, Planetary interiors

## Introduction

A fundamental problem hampering studies of the composition and structure of the terrestrial planets is that most of their mass is located at depths inaccessible to direct investigation. The occurrence and behavior of solid and molten silicate and metal phases at ambient pressures are relatively well constrained due to analyses of natural surface samples. For Earth, some additional insights into the chemical properties of the deeper subsurface can be obtained indirectly from analyses of natural samples of deep origin, such as extrusive volcanic rocks formed by partial melting of planetary mantles and magmatic minerals from deeper levels entrained in such rocks during their transport to the surface (e.g., [1–4]), high-pressure metamorphic rocks formed at great depths but subsequently exhumed to the surface in mountain belts (e.g. [5]), and the study of mineral inclusions in diamonds formed hundreds of kilometers underneath the surface (e.g., [3]). Seismology can also provide a window into the physical and chemical properties of planetary interiors but is currently limited to studies of the Earth (e.g. [6–8]) and the Moon (e.g. [9, 10]). Interior models for other planets and moons in the solar system are constrained by remote sensing and geodesic data obtained by space missions (e.g., [11–14]).

Correct interpretation of measured planetary characteristics for interior models relies on the understanding of high-pressure and high-temperature phase mineralogy. With the use of physical and chemical laws which govern the crystal structure of minerals,

e.g. thermodynamic relations and density functional theory, ambient-condition crystal-line properties can be extrapolated to high pressures and high-pressure phases can be predicted (e.g. [15, 16]). However, such methods become computationally expensive and impractical for systems containing numerous elements, and have difficulties in predicting material properties in the high-temperature regime of deep planetary interiors.

Experimental techniques that expose samples to high pressures and temperatures provide crucial complementary constraints on the matter of planetary interiors. For interior pressures to a maximum of approximately 3.5-4 GPa, a so-called piston cylinder press can be used to compress cubic millimeter sized natural or synthetic rock samples while simultaneously heating the samples to a maximum of approximately 1650 °C (e.g. [17]). Two such piston-cylinder apparatusi at Vrije Universiteit Amsterdam, the Netherlands, are currently part of the Distributed Planetary Simulation Facility (DPSF) of the EU Europlanet 2020 Research Infrastructure, providing access to European planetary scientists interested in using this technique. Facilities that can achieve higher pressures relevant for Earth's upper mantle and the deep interiors of the Moon, Mercury, Mars and Ganymede would help expand the opportunities of this scientific community.

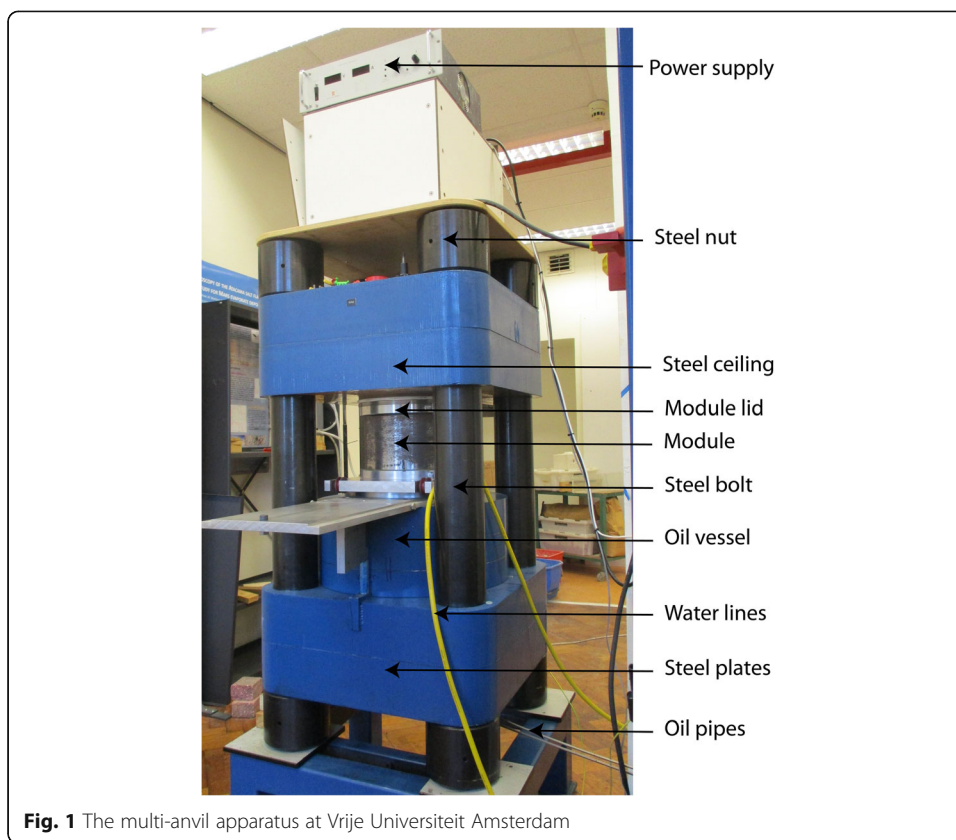
Here, we present the experimental setup and assembly pressure calibration of an 800 ton multi-anvil apparatus at the Vrije Universiteit Amsterdam, the Netherlands. This press can expose cubic millimeter-sized samples to pressures up to ~ 10 GPa and temperatures up to ~ 2100 °C with the assembly used in this study and significantly extends the pressure-temperature range that is available through international access to this facility.

Since the first introduction of multi-anvil presses more than half a century ago, developments of this type of presses have significantly improved their experimental reproducibility, extended the attainable pressure and temperature range, and hence expanded the corresponding research opportunities [18]. Although multi-anvil apparatusi are widely used for examining the physical and chemical characteristics of planetary materials, details of their calibration are rarely published, hampering full comparison of results obtained at different facilities. Here, we present full details of the calibration of the device, including an assessment of uncertainties.

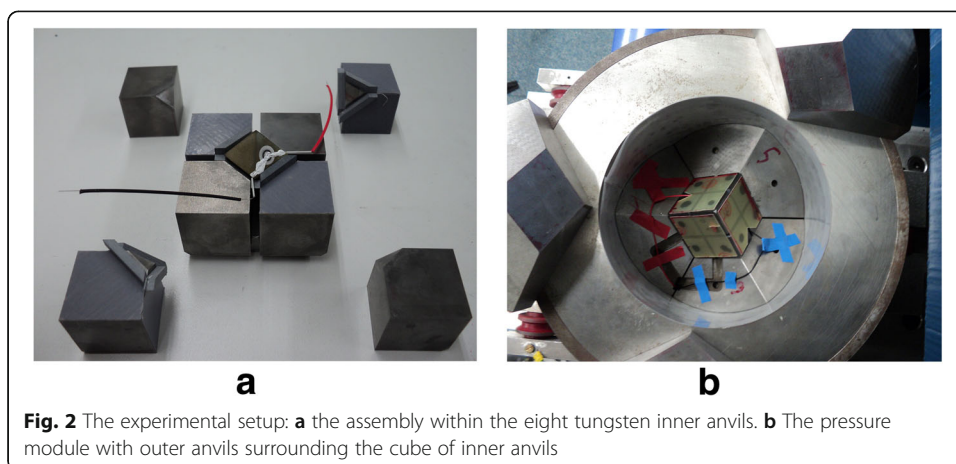
## **Methods/Experimental**

### **Experimental setup**

The 800 ton hydraulic press was built by the workshop of the Department of Earth Sciences at the University of Bristol, UK. The apparatus contains a Walker-type pressure module [19] with a 15 cm tall, 20 cm inner diameter, and 6.3 cm thick hardened steel wall that rests on an oil vessel. The module holds anvils in a Kawai geometry [20], consisting of six hardened steel outer wedges and eight cubic-inch-sized tungsten carbide (WC) inner anvils (grade THM-U, Kennametal, Arnhem, the Netherlands). A hardened steel module lid rests on the top three wedges and closes the module. An hydraulic pumping system regulates the pressure in the oil vessel, which controls the pressure in the module generated by pressing the module upward against a steel ceiling (Fig. 1). Mylar sheets (0.1 mm thickness), lubricated with polytetrafluorethylene (PTFE) spray, line the inner wall of the module and the outer surfaces of the outer wedges to reduce



friction and prevent electrical conductance between the wedges and the module wall [19]. All inner anvils have one truncated corner with 11 mm edge length (TEL = truncated edge length = 11 mm). They are cubically assembled and enclose an octahedral sample assembly with 18 mm edge lengths (OEL = octahedron edge length = 18 mm), leaving ~3.4 mm space in between the anvils (Fig. 2). Pyrophyllite gaskets of 3.3/3.0 mm height/width are placed between the inner anvils near the truncated edges to prevent contact between inner anvils and prohibit outward flow of the sample assembly's pressure medium during compression. PTFE tape is placed snugly against the back

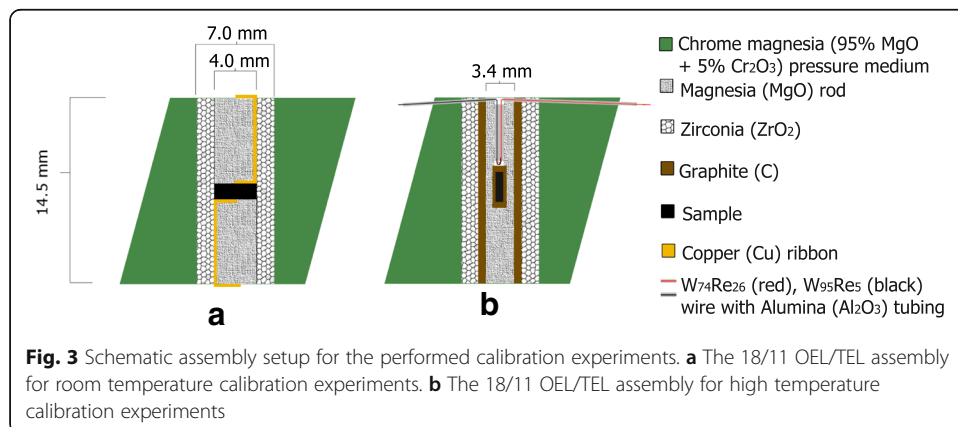


of the gaskets to minimize extrusion of these gaskets during compression. The cubically assembled inner anvils are covered and held together by sheets of epoxy resin fiberglass (known as G10 sheets, 0.65 mm thickness) glued on each side of the cubic assemble. These G10 sheets also prevent electrical conductance between the inner anvils and the outer wedges. Two copper foils are placed through cuts in the G10 sheets and electrically connect the bottom inner anvil with one of the lower wedges and the top inner anvil with one of the upper wedges. These yield electrically connected paths from the bottom octahedral surface to the module bottom plate and from the top octahedral surface to the module top plate, via the inner anvils, copper and wedges.

The sample assembly (Fig. 3) is a  $\text{Cr}_2\text{O}_3$ -doped MgO octahedron (95% MgO and 5%  $\text{Cr}_2\text{O}_3$  with 30% porosity, from Japan Ceramic Engineering Co., Ltd.), with a 7 mm diameter central hole [21]. A zirconia ( $\text{ZrO}_2$ ) sleeve of 4 mm inner diameter (drilled out of plates from Mino Yogyo Ceramics, Japan) is placed in the hole and acts as heat insulator for its interior. The assembly set-up interior to the  $\text{ZrO}_2$  sleeve varies depending on the type of experiment. In this study, sample pressures are calibrated with respect to the vessel's oil pressure by identifying and bracketing known high-pressure phase transitions. Electrical resistance measurements at room temperature are performed to detect high-pressure transitions in metals in situ. High-temperature quench (ex situ) experiments are performed to bracket high-pressure phase transitions in silica ( $\text{SiO}_2$ ) and in calcium germinate ( $\text{CaGeO}_3$ ).

For experiments that measure electrical resistance of a sample at room temperature, the  $\text{ZrO}_2$  sleeve contains two MgO rods that squeeze a sample of thin needle-like dimensions at the assembly's centre. Two copper ribbons are placed along the outside of the MgO rods to electrically connect the sample with the two opposite surfaces of the octahedral assembly and close the electrical path from the top to the bottom of the module through the sample (Fig. 3a). An ohmmeter measures the electrical resistance between the top and bottom of the module in situ during sample compression.

For high-temperature quench (ex situ) experiments, a graphite sleeve with 3.6 mm inner diameter is placed inside the zirconia and closes the electrical path from the top of the module to the bottom. A 2 mm long graphite sample bucket with a 1 mm thick lid contains the sample powder and is placed in the middle of the assembly, encapsulated by crushable polycrystalline MgO parts (Fig. 3b). Type C ( $\text{W}_{95}\text{Re}_5$  and  $\text{W}_{74}\text{Re}_{26}$ ) thermocouple wires are guided through alumina tubes to the sample and create a junction just above the sample container. An electrical voltage is applied by a DC power



supply (Delta Elektronika) between the top and bottom of the module to heat the sample environment by the ohmic dissipation in the graphite cylinder. The temperature difference between the thermocouple junction and the ends of the thermocouple wires induces a voltage at the thermocouple ends (the Seebeck effect). We measure this voltage and relate it to sample temperature using the ASTM E230/E230M standard from the National Institute of Standards and Technology (NIST).

### Starting materials and phase transitions

Room temperature resistance measurements are performed on metallic bismuth (Bi) samples (Alfa Aesar, 99.999% purity). Bismuth phase transitions from trigonal to monoclinic (Bi I-II) at  $2.55 \pm 0.006$  GPa, from monoclinic to tetragonal (Bi II-III) at  $2.69 \pm 0.01$  GPa, and from tetragonal to body-centered cubic (Bi III-V) at  $7.66 \pm 0.18$  GPa are historically well studied by a variety of methods including detecting changes in sample volume, shock measurements, detecting variations in electrical resistance and by crystal structure measurements using in-situ X-ray diffraction ([22]; and references therein). We identify the phase transitions by detecting characteristic variations in the measured electrical resistance during compression.

High temperature quench experiments are performed with  $\text{CaGeO}_3$  (synthesized to wollastonite structure) and hydrated  $\text{SiO}_2$  (Qtz structure) (Alfa Aesar) sample powders. At 1200 °C, a phase transition in  $\text{SiO}_2$  from trigonal ( $\alpha$ -) quartz to monoclinic coesite takes place at  $3.2 \pm 0.1$  GPa [23–29]. At 1300 °C, a phase transition from monoclinic coesite to tetragonal stishovite takes place in  $\text{SiO}_2$  at  $9.4 \pm 0.4$  GPa [23, 29–35]. At 1000 °C, a phase transition in  $\text{CaGeO}_3$  from tetragonal garnet to orthorhombic perovskite occurs at  $6.2 \pm 0.2$  GPa [36–41].

### Experimental procedure and sample analysis

After loading the sample assembly, pressure is increased at a rate of 20 bar per hour for high-temperature experiments and 10 bar per hour for room temperature experiments. For the latter, electrical resistance is measured continuously during this compression stage. After the target pressure is attained, high-temperature experiments are heated at a rate of 50 °C per minute to the target temperature. Temperature is held constant at the target value for a minimum of 30 min and up to a few hours. Samples are quenched by switching off the electrical power. When the experiment is finished, i.e. after target pressure is achieved for a room temperature experiment or when the module is cooled down to below 50 °C after a high-temperature experiment, pressure is reduced by 10 bar per hour to ambient conditions.

Quenched samples are embedded in a 1 in. epoxy mount and ground with alumina paper until the sample surface is exposed. We collected Raman spectra from these samples to determine the sample's mineralogy using a red (785 nm) laser on a Renishaw InVia Reflex confocal Raman microscope at Vrije Universiteit Amsterdam with a grating of 1200 grooves/mm.

## Results

### Sample analysis

The electrical resistance measured in-situ through a Bi sample during a room temperature, high-pressure experiment is plotted in Fig. 4. The detected variations in

electrical resistance identify the Bi I-II phase transition at an oil pressure of 89 bar, the Bi II-III phase transition at an oil pressure of 108 bar, and the Bi III-V phase transition at an oil pressure of 313 bar. These transitions are used as a first-order indication for the relation between sample pressure and oil pressure at high temperatures.

Raman spectra of quenched  $\text{SiO}_2$  samples, obtained from high-temperature quench experiments listed in Table 1, are shown in Fig. 5. Experiments MA16 and MA11 with oil pressures at 130 bar and 135 bar bracket the disappearance of quartz peaks at  $\sim 206 \text{ cm}^{-1}$  and  $\sim 464 \text{ cm}^{-1}$  and the appearance of coesite peaks at  $\sim 270 \text{ cm}^{-1}$  and  $\sim 520 \text{ cm}^{-1}$ . Experiments MA31 and MA33 with oil pressures at 390 bar and 420 bar bracket the disappearance of  $\sim 270 \text{ cm}^{-1}$  and  $\sim 520 \text{ cm}^{-1}$  peaks and the appearance of stishovite peaks at  $\sim 230 \text{ cm}^{-1}$  and  $\sim 752 \text{ cm}^{-1}$ .

Raman spectra of quenched  $\text{CaGeO}_3$  samples, obtained from high-temperature quench experiments listed in Table 1, are shown in Fig. 6. Both experiments MA30 at 255 GPa and MA23 at 260 GPa show clear garnet-structured peaks at  $508 \text{ cm}^{-1}$  and  $805 \text{ cm}^{-1}$  [40], which are absent in samples that were quenched at higher pressure. The perovskite-structure peak at  $284 \text{ cm}^{-1}$  [42] is present in MA23 and all samples that were quenched at higher pressure. The Raman spectrum of MA23 contains both the garnet and perovskite structure signatures and marks the location of the phase transition. Sample MA28, also obtained from an experiment at 260 bar, does not show any Raman signature for garnet. We go into more detail on this issue in the discussion section.

### Calibration curve

We obtain a pressure calibration curve by spline interpolation. The Bi phase transitions are not used in the interpolation, because they have been identified at room temperature whereas we are interested in the pressure calibration at high temperatures. Figure 7 plots the pressure calibration curve, of which Table 2 lists consecutive 0.5 GPa sample pressure points.

## Discussion

### Temperature errors

The temperature distribution in high-pressure assemblies is known to be heterogeneous in axial and radial dimensions. In our experiments, temperature is measured by

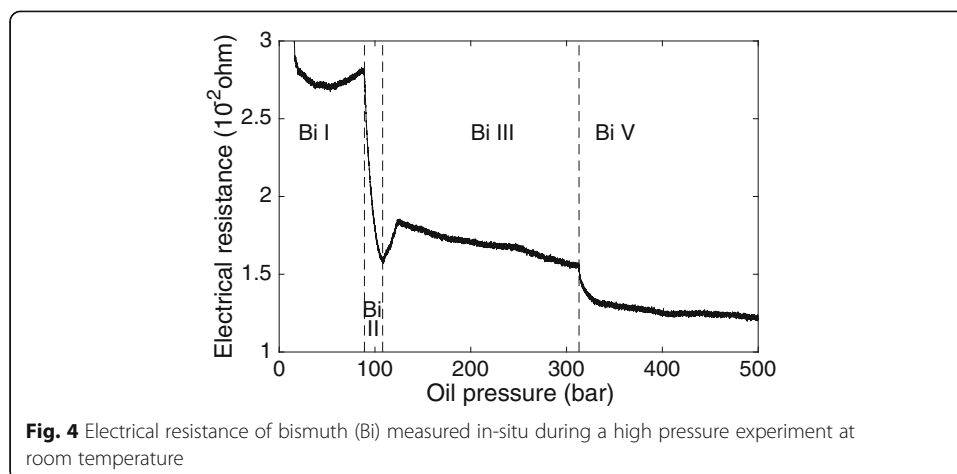
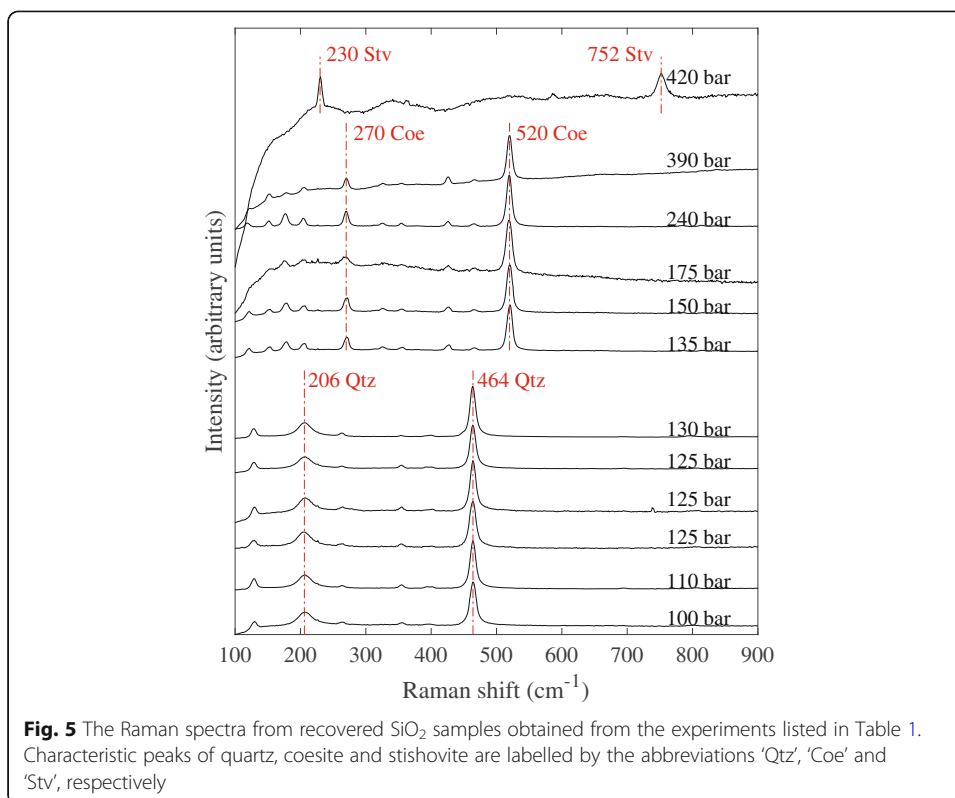


**Table 1** <sup>a</sup>Thermocouple readout failed in these experiments. These temperatures have been estimated based on the power-temperature relationship of other experiments at similar pressures and carry an uncertainty of  $\pm 150$  degrees

Experiment	Starting composition	Oil pressure (bar)	Power (W)	Temperature (°C)	Duration (hr:min)	Resulting polymorph
MA2	SiO <sub>2</sub>	240	700	1100 <sup>a</sup>	3:00	Coe
MA4	SiO <sub>2</sub>	300	500	750 <sup>a</sup>	2:50	Coe
MA5	SiO <sub>2</sub>	175	500	750 <sup>a</sup>	3:30	Coe
MA6	SiO <sub>2</sub>	175	844	1100	1:50	Coe
MA7	SiO <sub>2</sub>	150	773	1200	3:30	Coe
MA8	SiO <sub>2</sub>	100	805	1200 <sup>a</sup>	2:00	Qtz
MA9	SiO <sub>2</sub>	125	755	1200 <sup>a</sup>	1:00	Qtz
MA11	SiO <sub>2</sub>	135	766	1200	3:30	Coe
MA13	SiO <sub>2</sub>	110	682	1200	5:00	Qtz
MA14	SiO <sub>2</sub>	125	665	1200 <sup>a</sup>	2:00	Qtz
MA15	SiO <sub>2</sub>	125	674	1200	2:00	Qtz
MA16	SiO <sub>2</sub>	130	717	1200	6:00	Qtz
MA23	CaGeO <sub>3</sub>	260	574	950 <sup>a</sup>	1:30	Grt + Prv
MA24	CaGeO <sub>3</sub>	300	695	1000 <sup>a</sup>	1:35	Prv
MA25	CaGeO <sub>3</sub>	280	667	1000 <sup>a</sup>	1:10	Prv
MA26	CaGeO <sub>3</sub>	270	742	1000	1:20	Prv
MA27	CaGeO <sub>3</sub>	265	651	1000	1:30	Prv
MA28	CaGeO <sub>3</sub>	260	895	1000	1:00	Prv
MA29	CaGeO <sub>3</sub>	263	650	1000 <sup>a</sup>	1:00	Prv
MA30	CaGeO <sub>3</sub>	255	670	1000 <sup>a</sup>	1:05	Grt
MA31	SiO <sub>2</sub>	390	982	1300	0:30	Coe
MA33	SiO <sub>2</sub>	420	878	1300	1:00	Stv

a thermocouple at the wire-junction just outside the graphite sample container, approximately 1.5 mm away from the center of the assembly and sample. For an indication on the temperature difference between the sample and the thermocouple junction as well as the extent of thermal heterogeneity, we have modelled the temperature distribution in our assembly using the numerical method of Hernlund et al. [43]. The temperature distribution in the assembly is assumed to be axisymmetric about the central axis of the assembly (the  $r = 0$  line) and symmetric about the assembly's horizontal mid-plane (the  $z = 0$  plane), where zero heat flux boundary conditions are applied. Constant temperature boundary conditions are applied at  $z = 11$  mm and  $r = 11$  mm of un-prescribed value, which is interior to the WC cubes and far from the assembly's center. We used the model setting that accounts for the effect of the surrounding module, which prescribes a constant boundary temperature of 25 °C several hundreds of millimetres away from the sample [43]. A thermocouple temperature of 1200 °C was assumed.

The results indicate that temperatures interior to the graphite heater vary most strongly in axial direction (Fig. 8). This temperature gradient is small interior to the graphite sample container ( $z < 1.5$  mm), because graphite has a high thermal conductivity. The temperature at the thermocouple junction (at  $z = 1.5$ ), is only six degrees below the central temperature of 1200 °C according to this numerical model. These modelled

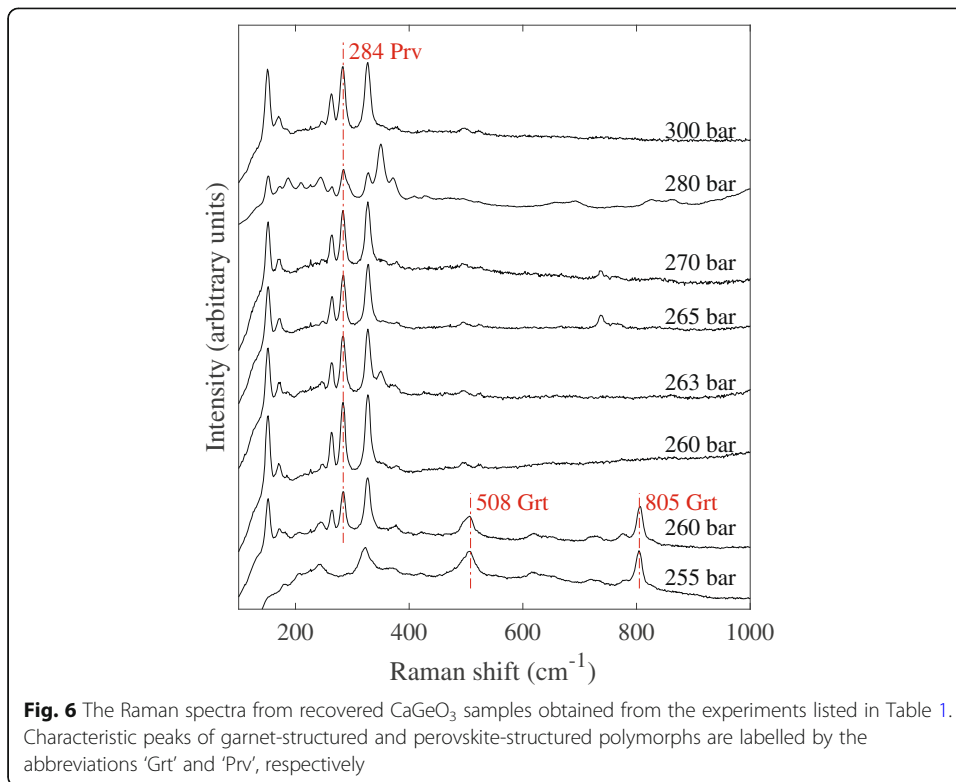


variations are consistent with the  $< 20$  °C variations in the central 3 mm of the assembly measured by van Westrenen et al. [44] using spinel growth kinetics in a similar assembly. The modelled temperature drops by 90 °C from  $z = 1.5$  mm to  $z = 2.5$  mm, illustrating the importance of placing the thermocouple junction close to the sample container. In practice, the hard 4-bore Al<sub>2</sub>O<sub>3</sub> tube holding the thermocouple wires is usually effectively pressing the thermocouple junction onto the graphite bucket while it is pressurized by the WC anvils, which ensures that the junction is usually at or very close to the boundary between the sample container and Al<sub>2</sub>O<sub>3</sub> tubing. This implies that the temperature read-out is usually fairly accurate, provided that the total length of the sample and container combination is below 3 mm in  $z$ -direction.

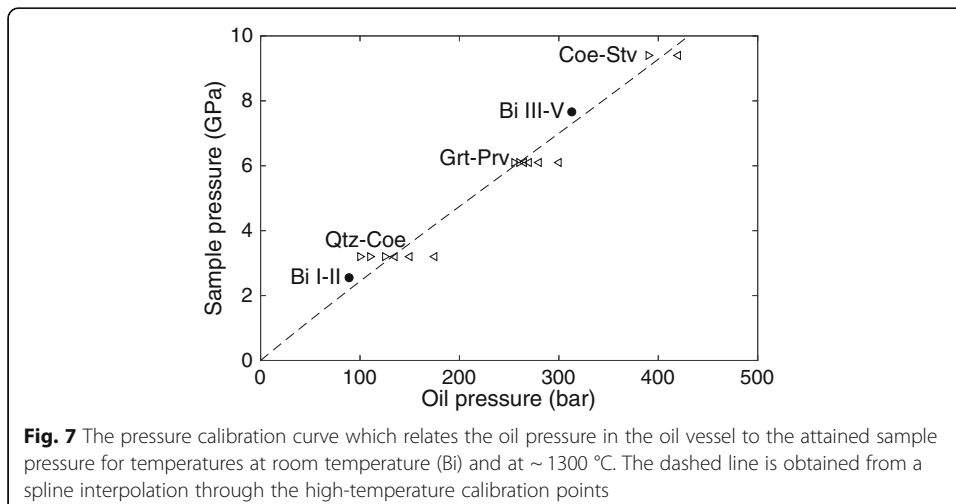
An additional error on the temperature measurement arises from the pressure effect on the electromotive force induced by the Seebeck effect that is not taken into account (the ASTM E230/E230M standard is calibrated at ambient pressures). This pressure effect on the thermocouple is expected to be small at temperatures below 1500 °C and is universally neglected in high-pressure setups around the world [45].

Table 1 shows that a significant number of experiments experienced thermocouple failure. This is particularly the case for the earlier experiments (numbered MA25 and lower), of which 60% had failed thermocouples. In these early experiments, we used thermocouple wires of 0.018 mm diameter. The later experiments, numbered MA26 and beyond, were performed with slightly thicker thermocouple wires of 0.025 mm thickness, which help prevent thermocouple failures (28% thermocouple failure). We are currently taking additional measures to further reduce thermocouple failures.





In experiments where thermocouple readout failed, the sample temperature is estimated by the relation between power and temperature as recorded in comparable experiments with surviving thermocouples (Fig. 9). The power-temperature relation varies per experiment for several reasons. First, while our calibration work progressed, we were increasingly successful in machining thinner graphite heaters which heat more efficiently. This is reflected in Fig. 9 by the lower temperature in the MA6, MA7, and MA11 experiments compared to the MA13, MA15 and MA16 experiments at similar powers. Second, heating is less efficient at higher pressures, which is reflected by the lower temperature in the experiments from MA26 to MA32 at similar power compared



**Table 2** A list of points on the calibration curve

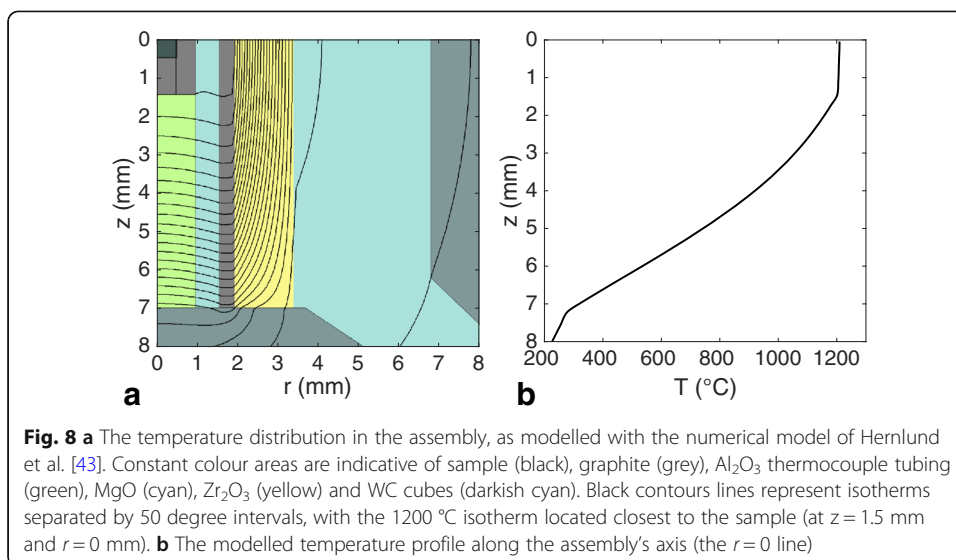
Oil pressure (bar)	Sample pressure (GPa)
21	0.5
41	1
62	1.5
83	2
104	2.5
125	3
146	3.5
168	4
190	4.5
212	5
234	5.5
257	6
279	6.5
301	7
323	7.5
345	8
367	8.5
389	9
410	9.5
431	10

to the MA13, MA15 and MA16 experiments. We took these effects into consideration when we estimated the temperature of experiments with failed thermocouples. The resulting errors on these estimates are likely on the order of  $\pm 150$  degrees. The power used in experiment MA28 is exceptionally high in relation to those of other experiments at similar pressures, in particular in relation to experiment MA23 that was performed at identical pressure. We suspect that the temperature measurement of the MA28 experiment was in error by  $\sim 200$  °C (too low), potentially as a result of a rare displacement of the thermocouple junction away from the sample container. This may have placed MA23 at the garnet-perovskite boundary and the hotter MA28 in the stability field of perovskite.

### Pressure errors

The phase transitions used for the high-temperature quench experiments are relatively insensitive to temperature. We estimate that the temperature error propagates to an error in the pressure calibration of below 0.2 GPa.

The largest error of our pressure calibration originates from uncertainties in the pressure of the phase transitions themselves. These errors accumulate with increasing pressure because fully hydrostatic experiments (when samples pressure can be directly calculated by the amount of applied force) can only be performed at pressures below  $\sim 3$  GPa, as most appropriate liquid pressure media will accumulate stresses at higher pressures (e.g. [22]). A pressure standard for experimental studies for higher pressure phase relations relies on the extrapolation of crystalline behavior at low pressures using

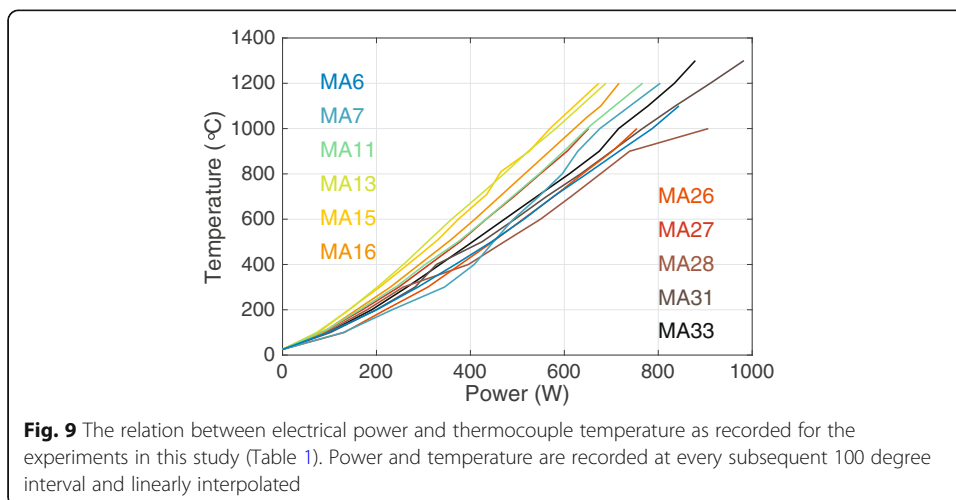


thermodynamic formulations (equations of state). The errors on these extrapolations increase with increasing pressure. As a result, the standard error on the phase transitions used in this study are below  $\pm 0.1$  GPa for the Bi I-II transition,  $\pm 0.2$  GPa for the quartz-coesite transition in SiO<sub>2</sub> and the garnet-perovskite transition in CaGeO<sub>3</sub>,  $\pm 0.3$  GPa for the Bi III-V transition and  $\pm 0.4$  GPa for the coesite-stishovite transition in SiO<sub>2</sub>.

Another error originates from the identification of and interpolation between the calibration points. This error is difficult to quantify, but likely does not exceed 0.3 GPa. The total error on the pressure calibration grows from  $\pm 0.2$  GPa at 100 bars to  $\pm 0.6$  GPa at 400 bars.

### Conclusions

The 18/11 assembly as calibrated in this study can expose cubic millimeter sized samples to pressure and temperature conditions that exist in deep planetary interiors (down to a depth of  $\sim 300$  km in Earth,  $\sim 650$  km in Mercury and  $\sim 750$  km in Mars).



The apparatus can be used to test high-pressure phase relations predicted by ab initio and thermodynamic calculations (e.g. [15, 16]), and to give insights into the origin of surface material that is thought to originate from great depths. These types of experimental constraints on deep planetary matter are complementary to other approaches currently adopted in interior planetary modeling studies ([11–14]). In the future, a smaller 8 mm / 3 mm OEL/TEL assembly can be used in the same press expanding the accessible pressure range to a maximum of ~ 25 GPa (e.g. [21]).

#### Abbreviations

Coe: Coesite; Grt: Garnet; OEL: Octahedral edge length; Prv: Perovskite; Qtz: Quartz; Stv: Stishovite; TEL: Truncated edge length

#### Acknowledgements

We thank Yingwei Fei of the Geophysical Laboratory at the Carnegie Institution for Science in Washington DC, and Stephan Klemme and Arno Rorhbach from the Universität Münster for providing assembly parts for experiments at times that we were in need.

#### Funding

This research was funded by a Netherlands Space Office User Support Programme Space Research grant (ALW-GO/12-38) to W.v.W. and the Belgian Science Policy Office (contract BR/143/A2/COME-IN). Europlanet 2020 RI has received funding from the European Union's Horizon 2020 research and innovation programme under grant agreement No 654208.

#### Availability of data and materials

Data is available upon request to the corresponding author.

#### Authors' contributions

JSK has done most of the writing and figures of this paper, followed by SML and WvW. JSK and SML have performed most of the experiments in this study. RS and DMvH have constructed the necessary oil-pumping system and its regulations. WvdP has installed the necessary electricity system and its regulations. NR has been involved in the early stages of the installation of this device. RJvdG has helped moving the 800-ton press and manufactured crucial assembly-parts. ESS has performed a few experiments and was the line of communication to the University of Münster for requesting assembly-parts at times that we were in need. WvW, JSK and SML have managed the whole operation from installation to calibration of the press. All authors read and approved the final manuscript.

#### Competing interests

The authors declare that they have no competing interests.

#### Publisher's Note

Springer Nature remains neutral with regard to jurisdictional claims in published maps and institutional affiliations.

#### Author details

<sup>1</sup>Faculty of Science, Vrije Universiteit Amsterdam, Amsterdam, the Netherlands. <sup>2</sup>Department of Earth Sciences, Indian Institute of Technology Roorkee, Roorkee, India.

Received: 16 April 2018 Accepted: 21 June 2018

Published online: 04 July 2018

#### References

1. Klaver M, de Roeber EWF, Nanne JAM, Mason PRD, Davies GR (2015) Charnockites and UHT metamorphism in the Bakhuis Granulite Belt, western Suriname: evidence for two separate UHT events. *Precambrian Res* 262:1–19 <https://doi.org/10.1016/j.precamres.2015.02.014>
2. Klaver M, Carey S, Nomikou P, Smet I, Godelitsas A, Vroon P (2016) A distinct source and differentiation history for Kolumbo submarine volcano, Santorini volcanic field, Aegean arc. *Geochem Geophys Geosyst* 17:3254–3273 <https://doi.org/10.1002/2016GC006398>
3. Koornneef JM, Gress MU, Chinn IL, Jelsma HA, Harris JW, Davies GR (2017) Archean and Proterozoic diamond growth from contrasting styles of large-scale magmatism. *Nat Commun* 8:1–8 <https://doi.org/10.1038/s41467-017-00564-x>
4. Nikogosian I, Ersoy Ö, Whitehouse M, Mason PRD, de Hoog JCM, Wortel R, van Bergen MJ (2016) Multiple subduction imprints in the mantle below Italy detected in a single lava flow. *Earth Planet Sci Lett* 449:12–19 <https://doi.org/10.1016/j.epsl.2016.05.033>
5. Hacker BR, Gerya TV, Gilotti JA (2013) Formation and exhumation of ultrahigh-pressure terranes. *Elements* 9:289–293 <https://doi.org/10.2113/gselements.9.4.289>
6. Rawlinson N, Pozgay S, Fishwick S (2010) Seismic tomography: a window into deep earth. *Phys Earth Planet Inter* 178:101–135 <https://doi.org/10.1016/j.pepi.2009.10.002>

7. Vissers RLM, van Hinsbergen DJJ, van der Meer DG, Spakman W (2016) Cretaceous slab break-off in the Pyrenees: Iberian plate kinematics in paleomagnetic and mantle reference frames. *Gondwana Res* 34:49–59 <https://doi.org/10.1016/j.jgr.2016.03.006>
8. de Wit RWL, Trampert J (2015) Robust constraints on average radial lower mantle anisotropy and consequences for composition and texture. *Earth Planet Sci Lett* 429:101–109 <https://doi.org/10.1016/j.epsl.2015.07.057>
9. Garcia RF, Gagnepain-Beyreix J, Chevrot S, Lognonné P (2011) Very preliminary reference moon model. *Phys Earth Planet Int* 188:96–113 <https://doi.org/10.1016/j.pepi.2011.06.015>
10. Weber RC, Lin PY, Garnero EJ, Williams Q, Lognonné P (2011) Seismic detection of the lunar core. *Science* 331: 309–312 <https://doi.org/10.1126/science.1199375>
11. Knibbe JS, van Westrenen W (2015) The interior configuration of planet mercury constrained by moment of inertia and planetary contraction. *J Geophys Res Planets* 120:1904–1923 <https://doi.org/10.1002/2015JE004908>
12. Orué HMJ, Vermeersen BLA (2016) Tides on Jupiter's moon Ganymede and their relation to its internal structure. *Neth J Geosci* 95:191–201 <https://doi.org/10.1017/njg.2015.23>
13. Rivoldini A, Van Hoolst T (2013) The interior structure of mercury constrained by the low-degree gravity field and the rotation of mercury. *Earth Planet Sci Lett* 377–378:62–72 <https://doi.org/10.1016/j.epsl.2013.07.021>
14. Root BC, Ebbing J, van der Wal W, England RW, Vermeersen LLA (2016) Comparing gravity-based to seismic-derived lithospheric densities: a case study of the British Isles and surrounding areas. *Geophys J Int* 208:1796–1810 <https://doi.org/10.1093/gji/ggw483>
15. Cottenier S, Probert MIJ, Van Hoolst T, Van Speybroeck V, Waroquier M (2011) Crystal structure prediction for iron as inner core material in heavy terrestrial planets. *Earth Planet Sci Lett* 312:237–242 <https://doi.org/10.1016/j.epsl.2011.09.045>
16. Jacobs MHG, Schmid-Fetzer R, van den Berg AP (2017) Phase diagrams, thermodynamic properties and sound velocities derived from a multiple Einstein method using vibrational densities of states - an application to MgO–SiO<sub>2</sub>. *Phys Chem Miner* 44:43–62 <https://doi.org/10.1007/s00269-016-0835-4>
17. McDade P, Wood BJ, van Westrenen W, Brooker R, Gudmundsson G, Souldar H, Najorka J, Blundy J (2002) Pressure corrections for a selection of piston-cylinder cell assemblies. *Min Mag* 66:1021–1028 <https://doi.org/10.1180/0026461026660074>
18. Liebermann RC (2011) Multi-anvil, high pressure apparatus: a half-century of development and progress. *High Pressure Res* 31:493–532 <https://doi.org/10.1080/08957959.2011.618698>
19. Walker D, Carpenter MA, Hitch CM (1990) Some simplifications to multianvil devices for high pressure experiments. *Am Mineral* 75:1020–1028 <http://ammin.geoscienceworld.org/content/75/9-10/1020>
20. Kawai N, Endo S (1970) The generation of ultrahigh hydrostatic pressures by a split sphere apparatus. *Rev Sci Instrum* 41:1178–1181 <https://doi.org/10.1063/1.1684753>
21. Leinenweber KD, Tyburczy JA, Sharp TG, Soignard E, Diedrich T, Petuskey WB, Mosenfelder JL (2012) Cell assemblies for reproducible multi-anvil experiments (the COMPRES assemblies). *Am Mineral* 97:353–368 <https://doi.org/10.2138/am.2012.3844>
22. Decker DL, Basset WA, Merrill L, Hall HT, Barnett JD (1972) High-pressure calibration: a critical review. *J Phys Chem Ref Data* 1:773–836 <https://doi.org/10.1063/1.3253105>
23. Akaogi M, Navrotsky A (1984) The quartz-coesite-stishovite transformations: new calorimetric measurements and calculation of phase diagrams. *Phys Earth Planet Int* 35:124–134 [https://doi.org/10.1016/0031-9201\(84\)90013-X](https://doi.org/10.1016/0031-9201(84)90013-X)
24. Bohlen SR, Boettcher AL (1982) The quartz - coesite transformation: a precise determination and the effects of other components. *J Geophys Res Solid Earth* 87:7073–7078 <https://doi.org/10.1029/JB087iB08p07073>
25. Bose K, Ganguly J (1995) Quartz-coesite transition revisited: reversed experimental determination at 500–1200 °C and retrieved thermochemical properties. *Am Mineral* 80:231–238 <https://doi.org/10.2138/am-1995-3-404>
26. Boyd FR, England JL (1967) The quartz-coesite transition. *J Geophys Res* 65:749–756 <https://doi.org/10.1029/JZ065i002p00749>
27. Coes L (1953) A new dense crystalline silica. *Science* 118:131–132 <https://doi.org/10.1126/science.118.3057.131>
28. Mirwald PW, Massonne HJ (1980) The low-high quartz and quartz-coesite transition to 40 kbar between 600° and 1600°C and some reconnaissance on the effect of NaAlO<sub>2</sub> component on the low quartz-coesite transition. *J Geophys Res Solid Earth* 85:6983–6990 <https://doi.org/10.1029/JB085iB12p06983>
29. Weaver JS, Chipman DW, Takahashi T (1979) Comparison between thermochemical and phase stability data for the quartz-coesite-stishovite transformations. *Am Mineral* 64:604–614. <https://pubs.geoscienceworld.org/msa/ammin/article-abstract/64/5-6/604/41027/comparison-between-thermochemical-and-phase>
30. Akimoto S (1972) The system MgO-FeO-SiO<sub>2</sub> at high pressures and temperatures - phase equilibria and elastic properties. *Tectonophysics* 13:161–187 [https://doi.org/10.1016/0040-1951\(72\)90019-4](https://doi.org/10.1016/0040-1951(72)90019-4)
31. Akimoto S, Syono Y (1969) Coesite-Stishovite transition. *J Geophys Res* 74:1653–1659 <https://doi.org/10.1029/JB074i006p01653>
32. Stishov SM, Popova SV (1961) A new dense modification of silica. *Geokimiya* 10:837–839
33. Yagi T, Akimoto S (1976) Direct determination of coesite-stishovite transition by in-situ X-ray measurements. *Tectonophysics* 35:259–270 [https://doi.org/10.1016/0040-1951\(76\)90042-1](https://doi.org/10.1016/0040-1951(76)90042-1)
34. Zhang J, Li B, Utsumi W, Liebermann RC (1996) In situ X-ray observations of the coesite-stishovite transition: reversed phase boundary and kinetics. *Phys Chem Miner* 23:1–10 <https://doi.org/10.1007/BF00202987>
35. Zhang J, Liebermann RC, Gasparik T, Harzberg CT, Fei Y (1993) Melting and subsolidus relations of SiO<sub>2</sub> at 9–14 GPa. *J Geophys Res* 98:19785–19793 <https://doi.org/10.1029/93JB02218>
36. Ono S, Kikigawa T, Higo Y (2011) In situ observation of a garnet/perovskite transition in CaGeO<sub>3</sub>. *Phys Chem Miner* 38:735–740 <https://doi.org/10.1007/s00269-011-0446-z>
37. Prewitt CT, Sleight AW (1969) Garnet-like structures of high-pressure cadmium germanate and calcium germanate. *Science* 163:386–387 <https://doi.org/10.1126/science.163.3865.386>
38. Ringwood AE, Major A (1967) Some high-pressure transformations of geophysical significance. *Earth Planet Sci Lett* 2:106–110 [https://doi.org/10.1016/0012-821X\(67\)90109-4](https://doi.org/10.1016/0012-821X(67)90109-4)
39. Ringwood AE, Seabrook M (1963) High-pressure phase transformations in germanate pyroxenes and related compounds. *J Geophys Res* 68:4601–4609 <https://doi.org/10.1029/JZ068i015p04601>

40. Ross NL, Akaogi M, Navrotsky A, Susaki J, McMillan P (1986) Phase transitions among the CaGeO<sub>3</sub> polymorphs (wollastonite, garnet, and perovskite structures): studies by high-pressure synthesis, high-temperature calorimetry, and vibrational spectroscopy and calculation. *J Geophys Res Solid Earth* 91:4685–4696 <https://doi.org/10.1029/JB091iB05p04685>
41. Susaki J, Akaogi M, Akimoto S, Shimomura O (1985) Garnet-perovskite transformation in CaGeO<sub>3</sub>: in-situ X-ray measurements using synchrotron radiation. *Geophys Res Lett* 12:729–732 <https://doi.org/10.1029/GL012i010p00729>
42. Durben DJ, Wolf GH, McMillan PF (1991) Raman scattering of the high-temperature vibrational properties and stability of CaGeO<sub>3</sub> perovskite. *Phys Chem Min* 18:215–223 <https://doi.org/10.1007/BF00202573>
43. Hernlund J, Leinenweber K, Locke D, Tyburczy JA (2006) A numerical model for steady-state temperature distributions in solid-medium high-pressure cell-assemblies. *Am Mineral* 91:295–305 <https://doi.org/10.2138/am.2006.1938>
44. van Westrenen W, van Orman JA, Watson H, Fei Y, Watson EB (2003) Assessment of temperature gradients in multianvil assemblies using spinel layer growth kinetics. *Geochem Geophys Geosyst* 4:1036 <https://doi.org/10.1029/2002GC000474>
45. Li J, Hadjilacos C, Mao HK, Fei Y, Hemley RJ (2002) Behavior of thermocouples under high pressure in a multi-anvil apparatus. *High Pressure Res* 23:389–401 <https://doi.org/10.1080/0895795031000088269>

**Submit your manuscript to a SpringerOpen<sup>®</sup> journal and benefit from:**

- ▶ Convenient online submission
- ▶ Rigorous peer review
- ▶ Open access: articles freely available online
- ▶ High visibility within the field
- ▶ Retaining the copyright to your article

---

Submit your next manuscript at ▶ [springeropen.com](http://springeropen.com)

---